Numerical Thermo-Hydraulic Simulation of Infiltration and Evaporation of Small-Scale Replica of Typical Dike Covers

Ponzoni, Elisa; Cardoso, Rafaela; Jommi, Cristina

DOI
10.3390/app142210170

Publication date
2024

Document Version
Final published version

Published in
Applied Sciences

applied sciences

MDPI

Article

Numerical Thermo-Hydraulic Simulation of Infiltration and Evaporation of Small-Scale Replica of Typical Dike Covers

Elisa Ponzoni [1,2], Rafaela Cardoso [3,*] and Cristina Jommi [2,4]

[1] Dipartimento di Ingegneria Civile Architettura Territorio Ambiente e Matematica (DICATAM), Università di Brescia, 25133 Brescia, Italy; eli.ponzoni85@gmail.com
[2] Department of Geoscience and Engineering, Delft University of Technology, 2628 Delft, The Netherlands; c.jommi@tudelft.nl
[3] CERIS/IST, Instituto Superior Técnico, Department of Civil Engineering, Architecture and Environment, University of Lisbon, 1049-001 Lisboa, Portugal
[4] Department of Civil and Environmental Engineering, Politecnico di Milano, 20133 Milano, Italy
* Correspondence: rafaela.cardoso@tecnico.ulisboa.pt; Tel.: +351-21-841-84-22

Abstract: Measurements taken on a historical dike in the Netherlands over one year showed that interaction with the atmosphere led to oscillation of the piezometric surface of about 0.7 m. The observation raised concerns about the long-term performance of similar dikes and promoted a deeper investigation of the response of the cover layer to increasing climatic stresses. An experimental and numerical study was undertaken, which included an investigation in the laboratory of the unsaturated behavior of a scaled replica of the field cover. A sample extracted from the top clayey layer in the dike was subjected to eight drying and wetting cycles in a HYPROP™ device. Data recorded during the test provide an indication of the delayed response with depth during evaporation and infiltration. The measurements taken during this continuous dynamic process were simulated by means of a finite element discretization of the time-dependent coupled thermohydraulic response. The results of the numerical simulations are affected by the way in which the environmental loads are translated into numerical boundary conditions. Here, it was chosen to model drying considering only the transport of water vapor after equilibrium with the room atmosphere, while water in the liquid phase was added upon wetting. The simulation was able to reproduce the water mass balance exchange observed during four complete drying–wetting cycles, although the simulated drying rate was faster than the observed one. The numerical curves describing suction, the amount of vapor and temperature are identical, confirming that vapor generation and its equilibrium is control the hydraulic response of the material. Vapor generation and diffusion depend on temperature; therefore, correct characterization of the thermal properties of the soil is of paramount importance when dealing with evaporation and related non-steady equilibrium states.

Keywords: HYPROP; TH coupled analysis; suction; evaporation; non-steady equilibrium

Citation: Ponzoni, E.; Cardoso, R.; Jommi, C. Numerical Thermo-Hydraulic Simulation of Infiltration and Evaporation of Small-Scale Replica of Typical Dike Covers. *Appl. Sci.* **2024**, *14*, 10170. https://doi.org/10.3390/app142210170

Academic Editor: Syed Minhaj Saleem Kazmi

Received: 16 September 2024
Revised: 29 October 2024
Accepted: 30 October 2024
Published: 6 November 2024

1. Introduction

Flood protection in the Netherlands is assured by multiple levels of dikes. A majority of this dike network defending the country from internal waterways referred to as regional dikes, originates from the historic practice of land reclamation, with both dike body and foundation consisting of heterogeneous soft soil deposits, such as clays, peats and silts [1].

The outer and inner water levels of these dikes are almost constant in time, due to careful regulation of the waterway and polder water levels by the waterboards. Therefore, changes in the water content of the dike body depend on the interaction with the atmospheric boundary conditions and the activity of the vegetation [2,3]. To protect the body of the dike from extreme changes in water content, hence reducing the hazard of cracks and degradation phenomena, they are protected by a top clayey layer underlying the vegetated cover. The combination of a vegetated topsoil with a 50 cm-thick on average

clayey layer is claimed to be enough to avoid seasonal swelling or shrinkage, changes in unit weight and changes in the stress state [4,5]. However, measurements taken in the body of various regional dikes in recent years demonstrate that huge variations are possible under increasing climate pressure. For example, at the Leendert de Boerspolder site, where a stress test was carried out over more than one year, the data showed that despite the clayey top material, interaction with the atmosphere led to oscillations of the piezometric surface of about 0.7 m [6], which are extremely relevant compared to the total 1.9 m height of the water defense.

To better understand how the top clayey layer behaves under atmospheric stresses and provide the necessary information to analyze its influence on the time-dependent response of water defense, an experimental and numerical study was undertaken, which included an investigation in the laboratory of the unsaturated behavior of the top clayey layer subjected to drying and wetting cycles in a small physical model set up in a HYPROP™ device. Different from previous research, where HYPROP data were just used to derive an "average" water retention curve under simplifying assumptions, the test data were interpreted as a boundary value problem, fully dependent on space and time.

A novel test protocol was designed to simulate climate actions, aiming to mimic the behavior observed in the top layer of dikes in the field. Different samples retrieved from the upper part of the regional dike at the Leendert de Boerspolder were tested both upon drying and wetting under relatively controlled boundary conditions. In the device, which was chosen as a small replica of the field cover, two tensiometers allow for direct measurement of suction at two depths and provide an indication of the delayed response with depth during evaporation and infiltration. The total mass of the samples was continuously recorded as well as the temperature at the bottom of the samples. Given that these measurements are taken during a continuous dynamic process, their interpretation is not as straightforward as usually assumed. If the tested material is clay, the material properties (water retention and hydraulic conductivity) cannot be directly inferred from the test data. In fact, the assumption that the average of the two measured suction values equals the suction corresponding to the average water content of the sample is strongly debatable when testing soils with low hydraulic conductivity, where the water content profile is very far from being linear [7].

To overcome the oversimplifying assumptions, the tests were simulated numerically using CODE BRIGHT [8,9] by means of a finite element discretization of the time-dependent coupled thermohydraulic response of the sample, including both liquid and vapor phases. The numerical simulation allows analyzing the response of the soil sample in detail, and better inferring the inherent properties of the tested material. In the following section, the suggested combined experimental–numerical procedure is described, referring to one of the tests performed. Attention is devoted to a crucial choice in the numerical simulation, related to the translation of the environmental boundary conditions into numerical forcing functions at the boundary of the model.

2. Materials and Methods

2.1. Soil Investigated

The clayey material investigated was collected from the first 2.0 m of 10 cores from a regional dike in South Holland. Grading size distribution curves are presented in Figure 1, where fine percentages between 32% and 58% can be seen. The percentages of organic matter vary between 3% and 8% in weight. The volumetric weight of the particles varies between 25.5 kg/m^3 (in the presence of organic matter) and 26.2 kg/m^3, being the plastic and liquid limits of 23% and 55%, respectively. The soil is classified as OH according to Unified Soil Classification. In situ, the material dry volumetric weight ranges between 13.8 and 15.3 kg/m^3, with water content between 25% and 30% (degrees of saturation between 88% and 93%). Hydraulic saturated permeability, measured using standard triaxial equipment, was between 6×10^{-7} and 10^{-10} m/s.

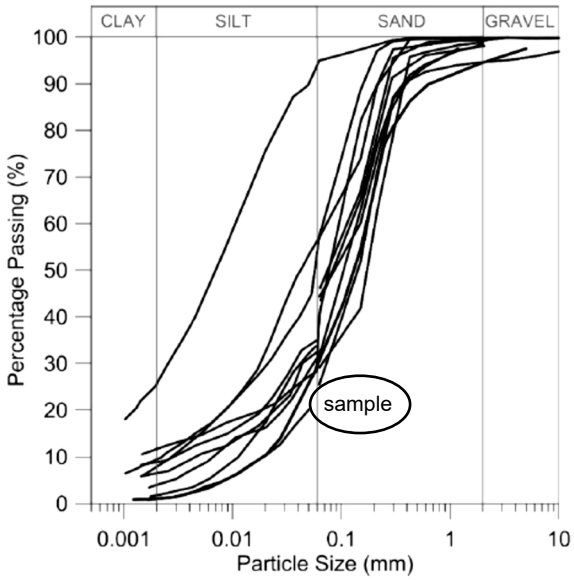

Figure 1. Grading size distribution of several samples of the soil.

The sample tested in this work was extracted from 0.85 m depth. Its dry volumetric weight was 13.8 kN/m^3, and it had a void ratio of 0.87 and water content of 30%, corresponding to a degree of saturation of 89%. Its grading size distribution curve is identified in Figure 1. This material can be representative because it is within the large majority of the curves of all samples collected.

2.2. Experimental Setup

The drying branch of the water retention curve (WRC) of the soil investigated was measured using HYPROP™ equipment (suctions below 80 kPa) and a Dew Point Potentiometer WP4C® (suctions between 1000 kPa and 100,000 kPa). The HYPROP™ was also used to test the soil upon drying and wetting, considering in situ behavior, with the advantage of allowing for relatively controlled boundary conditions (room with controlled relative humidity RH 50–55% and temperature 24–25 °C).

Due to the different measuring ranges of these two apparatuses, the complete soil water retention curve (WRC) was described, combining the results given by these two devices.

2.2.1. HYPROP

For the tests, a HYPROP™ device (HYdraulic PROPerty analyzer [10]) developed by UMS was used. It was developed to determine the water retention curve and the unsaturated conductivity of soils during desiccation. A saturated sample of soil is placed inside a container closed at the bottom and with the top opened to the atmosphere. The container has two tensiometers located at two different levels in the sample (shafts with 50 and 25 mm, and the tips are placed 32.5 and 12.5 mm from the inner base of the container; see Figure 2) and a temperature sensor.

Soil suction (water tension) is measured considering the water inside the shaft via a porous ceramic tip (Al_2O_3 porous sintered material, with air entry value of 800 kPa) and measured by a pressure transducer placed in the base. The measurement range of the tensiometers is from −85 kPa (water tension) to 2 kPa (water pressure), with 0.15 kPa accuracy in the range from 0 to −80 kPa. The temperature sensor can measure temperature between −30 and 70 °C, with a tolerance of ±0.2 K in the range of −10 to 30 °C.

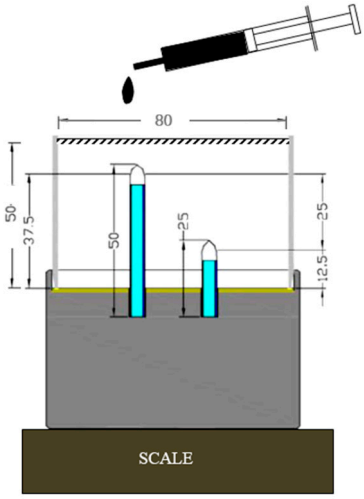

[mm]

Figure 2. Geometry of the HYPROP equipment and scheme illustrating the experimental setup adopted for wetting during the cycles.

The container is placed on a scale (measurement range from 0 to 2.5 kg and an accuracy of 0.1 g) and the total mass is recorded during the evaporation process, as well as suction measured with the two tensiometers and the temperature. The mass changes are then used to calculate the volumetric water content to be associated to the corresponding suction value, leading to the definition of the water retention curve. The measurements finish when one of the tensiometers runs dry or the mass difference becomes negligible.

Suction measurements using the HYPROP™ device were carried out in undisturbed samples extracted from core tubes (70 cm diameter). The specimens for the HYPROP equipment (a steel ring 80 mm diameter and 50 mm height) were trimmed using a cutting ring and removing the excess soil with a wire saw. The gap between the ring and the intact core (respectively, 80 and 70 mm in diameter) was filled with the same soil, trying to compact the material at the same natural density. Two holes were created in order to install the tensiometer shafts. These holes, each with the depth of the respective shaft and done using a specific tool, were filled with a slurry of the same soil while the shafts were not inserted. Six samples were tested.

The shafts were screwed into the sensor unit after being refilled with water and degassed in advance. Then, the sample was placed on the center of the HYPROP™ base unit in order to fit both shafts in the undisturbed part of the specimen. The ring containing the soil was carefully placed on a perforated plastic base covered by filter paper, then transferred into a tray filled with water and left in it overnight to saturate the sample. The dimensions and weight of each sample were taken before and after this procedure.

At the end of the test, each sample was measured and weighed before being oven-dried at 50 °C until reaching constant weight. Such temperature for drying was adopted due to the presence of organic matter in the soil (assuming that the amount of water removed was just within the pore space between the soil grains). This final weight allowed us to estimate the dry mass of the sample. All values of water content computed were related to the value after this drying (assumed to be null). The experimental procedure was designed specifically for this test, intending to simulate the exposition of climate actions.

2.2.2. WP4C

WP4C is a Water Dew Point Potentiometer developed by Decagon and measures the water potential using the chilled mirror dew point technique [11]. Suction measurement range is from 0 to −300,000 kPa with ±100 kPa accuracy to 0 to −10,000 kPa, with ±1% error for values between −10,000 and −300,000 kPa. A single point calibration is performed to ensure accurate measurements [12].

The dimensions of the samples for the Dew Point Potentiometer WP4C are around 37 mm in diameter and 4.5 mm in height. The samples are placed inside a closed chamber that has a fan, a mirror, a temperature sensor and a photoelectric cell. The fan is used to fasten vapor equilibrium between the air of the chamber and the soil pores. This photoelectric cell measures the exact point at which condensation first appears on the mirror, therefore detecting vapor pressure. The temperature is used to know the vapor pressure necessary to saturate the air, and therefore, the relative humidity RH is determined and can be used to compute the total suction Ψ using Kelvin's law:

$$s = -\frac{RT\rho}{M} ln(RH) \quad (1)$$

where M is the molecular mass of water (18.016 kg/kmol), ρ is the density of pure water (998 kg/m^3 at 293 K = 20 °C), R is the gas constant (8.314 J/mol^{-1}K^{-1}) and T is the absolute temperature.

The drying branch of the samples was characterized using WP4C, following HYPROP™ measurements [13]. The samples were dried in a temperature-controlled room (HR = 50–55% and T = 24–25 °C) and weighed along this process. After equilibrium to the new suction (controlled by weight), the samples were weighed before and after each measurement. Water content was found through these changes and confirmed by back analysis after knowing the final value measured after drying the sample in an oven under 50 °C. This is the standard procedure when using this equipment [13].

2.2.3. Test Simulating the Behavior of the Field Cover

The test simulating the behavior of the field cover was performed with the HYPROP™ equipment in which drying and wetting cycles were applied. Data were used to simulate the thermohydraulic-coupled behavior of the field cover. Drying was controlled to be below the maximum detection value of the tensiometers' operation and then wetting was applied, in which water was injected to the sample using a syringe (scheme in Figure 2). The amount of water added in the wetting stage was the same as that which was dried during the previous drying stage, measured by weight loss. This amount of water was spread on the top surface of the specimen, maintaining the same time interval between consecutive infiltrations. Wetting speed and time interval between the cycles were controlled, aiming to avoid desaturation of the tensiometers and also to characterize better the hydraulic hysteretic behavior of the material.

3. Experimental Results

3.1. Water Retention Curve

As experienced by Maček et al. [13], good and reliable results can be found by joining data from WP4C and HYPROP. This can be done if osmotic suction is considered negligible because WP4C measures total suction (matric plus osmotic) and HYPROP measures only matric suction. The complete drying branch of the WRC is presented in Figure 3a for the sample simulated in this paper. Similar curves were found for the other samples tested.

The HYPROP values are presented through continuous lines because data are recorded in a transient mode, while the tensiometers continuously adjust to changing boundary conditions (continuous drying from the top). The different readings of the two piezometers seen in Figure 3a result from their position at different levels. In contrast, WP4 measurements correspond to discrete points in the plot, as they are performed in static conditions once the sample is in equilibrium with the surrounding controlled environment.

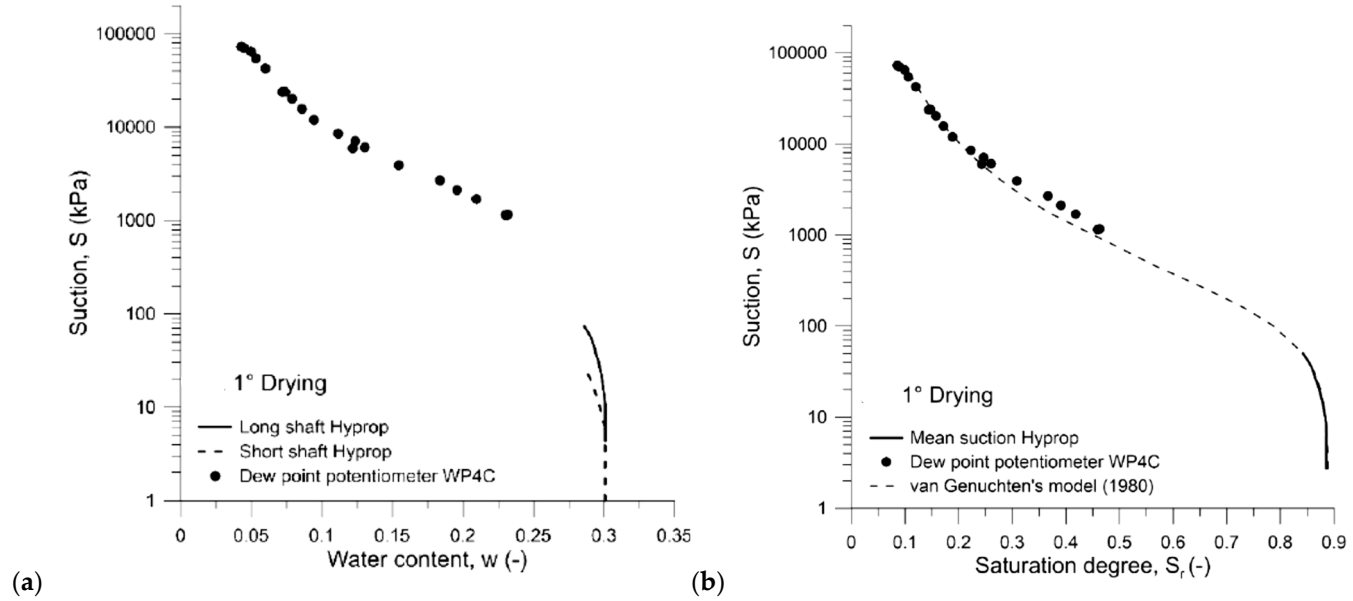

Figure 3. Water retention curve found using both equipment: (**a**) first drying, showing the HYPROP measurements for both tensiometers; (**b**) complete set of experimental points, using the average measurements of the two tensiometers and including the curves adjusted for using Equation (2).

It was assumed that osmotic effects were negligible because distilled water was used. In this case, the difference in the thermohydraulic boundary conditions described between HYPROP and WP4 during their readings is very important, and therefore, the points from each equipment may not be fitted by the same equation due to scattering. Nevertheless, and as observed in Figure 3b, considering the average values from the two tensiometers, it appears that the points can be aligned in the same branch, and therefore, all were used in the definition of the first drying branch of the water retention curve. These experimental points were fitted using the van Genuchten equation [14]:

$$S_r = \frac{G_s}{e} w = \left[1 + \left(\frac{s}{P}\right)^{\frac{1}{1-\lambda}}\right]^{-\lambda} (S_{r,max} - S_{r,res}) + S_{r,res} \quad (2)$$

where S_r is the degree of saturation, w is the gravimetric water content, e is void ratio (assumed constant, further explained), G_s is the specific gravity of soil solids, s is total suction, P and λ are constants and $S_{r,max}$ and $S_{r,res}$ are, respectively, the maximum and residual degrees of saturation. The parameters found for the sample considered in the numerical analysis are in Table 1 for the drying and wetting branches. Data from the first drying and last wetting were used and the envelope curves were used for model calibration.

Table 1. Calibration parameters of the WRC.

Parameter	Drying Branch	Wetting Branch
P (kPa)	0.15	0.03
λ	0.26	0.25

No volume changes were measured during the tests performed in any sample, confirming the observations during the saturation of unconfined samples, which are not presented here [15]. Therefore, the soil was assumed to be stiff during the hydraulic paths applied and changes in the degree of saturation were attributed to be solely due to changes in water content. This motivated the use of thermohydraulic-coupled analysis in this work to simulate experimental data, instead of thermo-hydro-mechanical analysis.

3.2. Cyclic Tests in the HYPROP Equipment

Figure 4 presents data measured in the test performed in the HYPROP equipment: inner and outer temperatures, relative humidity and changes in water mass and suction measured in the long and short shafts. In total, seven drying–wetting cycles were applied, followed by final drying.

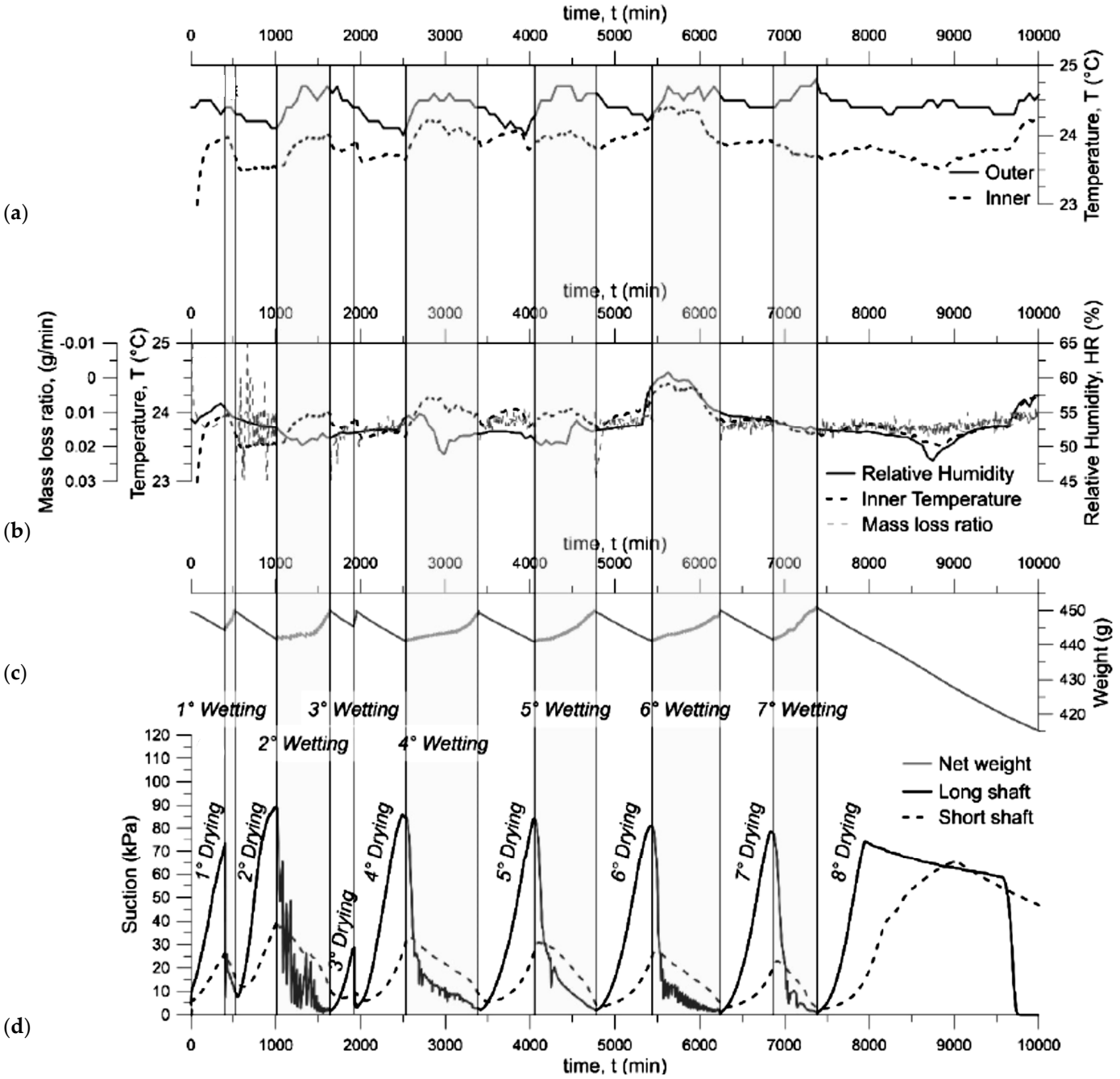

Figure 4. Data logged during drying and wetting cycles: (**a**) inner and outer temperature; (**b**) RH% and mass loss ratio; (**c**) net sample weight; (**d**) suction.

As shown in Figure 4, the variation of water mass decreased during drying due to evaporation and increased during wetting because it was added manually. It is worth noting that the temperature inside the sample increased relatively fast at the beginning of the test to reach the temperature of the room, probably because the water added was at room temperature and reached the bottom of the cell. After this initial increment, the inner temperature was kept approximately constant in the remaining test period.

Concerning suction, as expected, higher values were detected in the long shaft upon wetting because it is the tensiometer closest to the upper border in contact with the atmosphere. The suction recorded during the drying–wetting cycles applied allowed for quantifying hydraulic hysteresis, information necessary to be used later in the model simulation. Figure 5 presents the curves recorded during the drying–wetting cycles, respectively, in the long and short shafts. The curves at the final of each cycle do not coincide and it appears that a residual suction remains at the end of the test. This is because full saturation was not achieved in any wetting cycle due to the fact that the soil was not initially saturated and water was added only to compensate for water loss during drying.

Hysteresis was observed in both tensiometers' curves, but for the long shaft, the drying branch was above the following wetting branch, as usual, while in the short shaft, the wetting branch was above drying. This can be explained by transient readings and the delayed response of the short shaft because it is far from the sample surface, the upper boundary where water is being exchanged with the room atmosphere.

As when the water retention curve was fitted using Equation (2), the average values of the tensiometer readings were used to find the envelope curves of the cycles, and therefore fix the expressions of the two branches of the WRC to be used in the simulation, as well as hysteresis. The drying branch was defined considering the curve of the first drying, while the wetting branch was defined considering the curve of the last wetting. The slope of the transition between both was also determined to be used in the numerical model.

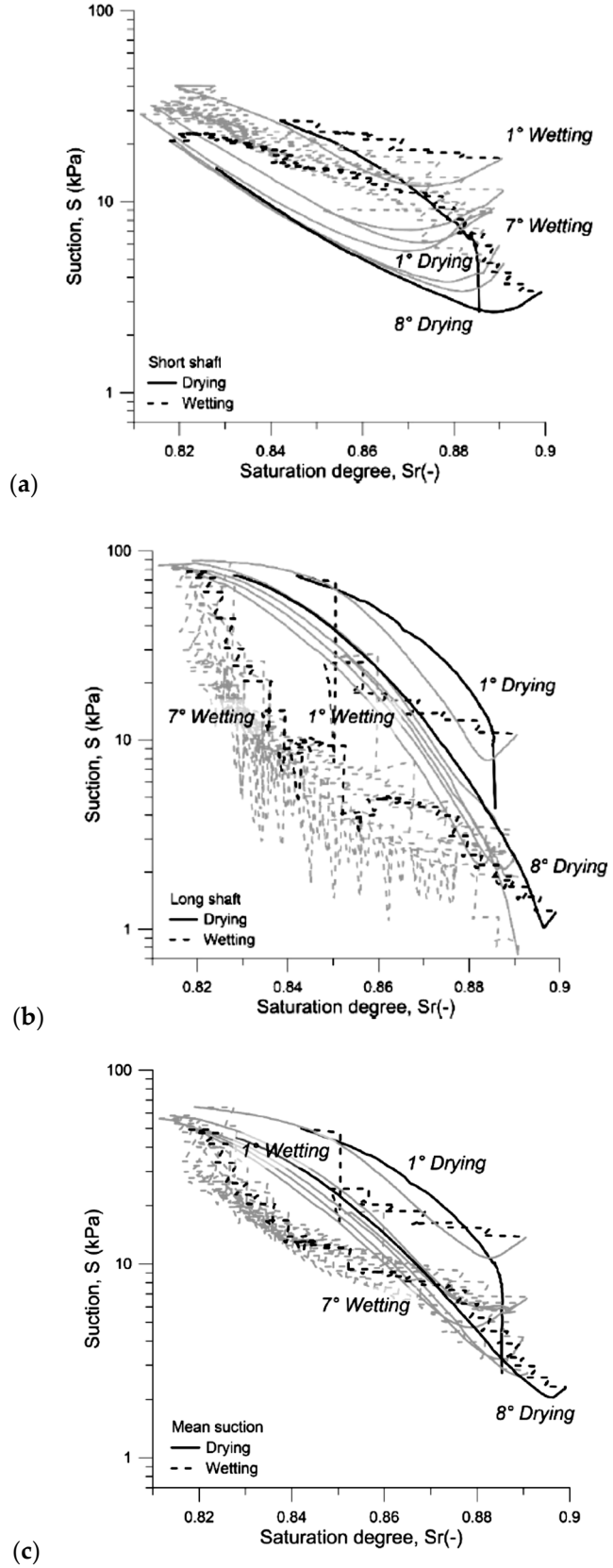

Figure 5. HYPROP measurements during the four drying–wetting cycles for the tensiometers (first cycle in black; last cycle in grey): (**a**) short shaft; (**b**) long shaft; (**c**) average values.

4. Numerical Simulation

4.1. Model Description

Program CODE BRIGHT® [8,9] was used to model the thermohydraulic behavior of the sample subjected to the first four drying–wetting cycles. The geometry of the HYPROP cell is presented in Figure 6, defined considering the axial symmetry around the *y*-axis of the cylindrical sample (80 mm diameter and 50 mm height). Two nodes, located at 15 mm from the *y*-axis and at 12.5 and 37.5 mm from the base, were defined to represent the position of the ceramic tips of the short and long tensiometers, respectively. The point at coordinates (0, 0) represents the location of the temperature sensor installed at the base. Triangular finite elements were used, also shown in Figure 6.

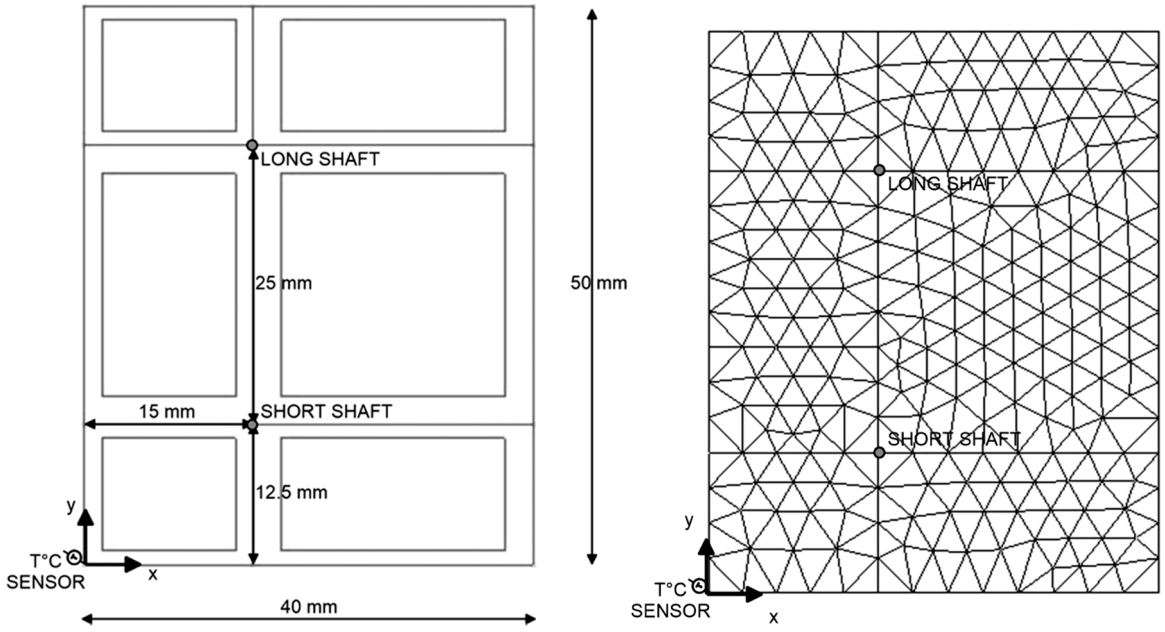

Figure 6. Discretization of the HYPROP sample using CODE BRIGHT (radial symmetry along *y*-axis).

CODE BRIGHT® is a finite element program that treats soils as porous deformable unsaturated media and solves a system of equations for the balance of the mass of solids, the mass of water (in liquid and gas phases), air (in gas phases and dissolved in water), and energy, and also considers stress equilibrium when mechanical loads are applied or when deformations caused by wetting occur. For this particular problem where water is added in the liquid phase and drying occurs by evaporation, with temperature changes during the process, it is fundamental to compute water flow in the liquid and gas phases (respectively, conduction and diffusion, advective and non-advective fluxes), as well as temperature changes. For this reason, the variables will be water pressure P_l and temperature T, both responsible for the balance between liquid water and the amount of vapor present. In addition, porosity is constant because the medium is assumed to be incompressible, and gas pressure P_g is assumed to be equal to atmospheric pressure (P_g = 0.1 MPa), which is also constant.

Initial values are therefore porosity n, temperature T^0, gas pressure ${P_g}^0$ and liquid pressure ${P_l}^0$, and the last is computed using initial suction s ($s = P_g - P_l$), measured with the tensiometers at the beginning of the test. The initial values adopted are in Table 2.

Table 2. Initial values for the model.

Porosity	P_g^0 (MPa)	P_l^0 (MPa)	Suction (MPa)
0.4661	0.1	0.095	0.005 (=$P_g - P_l$)

Concerning boundary conditions, although no mechanical load was applied, the vertical displacements were restrained at the base and horizontal displacements were restrained at the vertical side, corresponding to the lateral wall of the cell. Both the base and lateral walls were considered impervious but allowed for temperature exchanges.

4.2. Equations Solved

The balance of solid mass is obtained using Equation (3) [9], considering the porosity n and the volume of solid mass θ_s. The solid mass balance equation is naturally equal to zero because the quantity of solid particles in the system does not change. Porosity is also constant because there is no mechanical load applied and the material investigated is a non-swelling soil. In addition, volume changes due to temperature variations can be disregarded for the temperature intervals applied in the tests because they are very small.

$$\frac{\partial}{\partial t}[\theta_s(1-n)] = 0 \tag{3}$$

The balance of water is computed with Equation (4) [9]:

$$\frac{\partial}{\partial t}\left[\theta_l^w S_r n + \theta_g^w\right] + \nabla\cdot\left(j_l^w + j_g^w\right) = f^w \tag{4}$$

where water in the liquid and in the gas phases has θ_l^w and θ_g^w volumetric densities, respectively. S_r is the degree of saturation, obtained using the water retention curve (Equation (2), constants in Table 3), and f^w is the final water balance. Terms j_l^w and j_g^w are, respectively, the flux of water in the liquid phase (advective flux) and in the gas phase (vapor, non-advective flux).

Table 3. Hydraulic and thermal data.

Retention Curve (Drying Branch)				**Hysteresis (Transition to Wetting Branch)**		
P (MPa)	λ	Srl	Sls	dSr	P (MPa)	λ wetting
0.15	0.26	0	0.89	0.035	0.03	0.25
Intrinsic Permeability *		**Liquid Phase Relative Permeability**		**Conductive Flux of Heat**		
K (m^2)	n	A	Power l	λ_{dry} (W mK^{-1})	λ_{sat} (W mK^{-1})	
1.10×10^{-17}	0.4661	1	3	0.1	0.6	

* isotropic.

Flux j_l^w is caused by changes in liquid pressure P_l and is computed with Equation (5), where q_l is obtained by the generalized Darcy's law for the unsaturated case, given by Equation (6). In this equation, P_l is the liquid pressure already defined; ρ_l is the water density (1000 kg/m^3 at 20 °C); g is the acceleration of gravity (9.8 m/s^2); μ_l is the viscosity of water (8.9×10^{-7} kPa·s at 20 °C); k_{rl} is the liquid phase relative permeability, which represents the percentage of void area, which is filled with water (Equation (7), where A and λ are constants; see Table 3); and K is the intrinsic permeability (values in Table 3) obtained from the saturated permeability k_{sat} through Equation (8) [9].

$$j_l^w = \rho_l q_l \tag{5}$$

$$q_l = K\frac{k_{rl}}{\mu_l}(\nabla P_l - \rho_l g) \tag{6}$$

$$k_{rl} = AS_r^{\lambda} \tag{7}$$

$$K = \frac{k_{sat}\ \mu_l}{\rho_l} \sim \frac{k_{sat}}{10^7} \tag{8}$$

Flux j_g^w is the sum of a component computed using Darcy's law for gas (dry air and vapor) movement driven by changes in gas pressure and a component computed using Fick's law (Equation (9)) for molecular diffusion and dispersion. In this work, gas pressure is assumed to be constant and equal to the atmospheric pressure and dispersion is disregarded for simplification, and therefore, vapor transport only by diffusion is considered. In Equation (9), τ is a tortuosity parameter (τ = 1 default value), ρ_g is the gas density, D_g^{vap} is molecular vapor diffusion coefficient (Equation (10)) and ω_g^w is vapor mass fraction. The molecular vapor diffusion is given by Equation (10), where T is temperature (°C), P_g is gas pressure (P_g = 100 kPa) and D is a constant ($D = 5.9 \times 10^{-6}$ $m^2s^{-1}K^{-2.3}Pa$) [9].

$$j_g^w = i_g = -n\tau\rho_g(1 - S_r)D_g^{vap}\nabla\omega_g^w \tag{9}$$

$$D_g^{vap} = D\left[\frac{(273.15 + T)^{2.3}}{P_g}\right] \tag{10}$$

It is worth noting that the amount of vapor present or the mass of water in the gas phase, $\rho_{vap} = \rho_g\omega_g^w$, is found using the psychrometric law (Equation (11)) to compute vapor pressure p_{vap}, adopting a constant ρ_g = 0.01 g/cm^3 for dry air and water vapor as an ideal gas (ideal gas law, Equation (12), where R is constant, R = 8.315 J/mol·K and M is the molecular mass of water, M = 0.018 kg/mol). It is temperature-dependent.

$$p_{vap} = 136075exp\left(-\frac{5239.7}{273.15 + T}\right) \tag{11}$$

$$\rho_{vap} = \frac{p_v M}{R(273.15 + T)} \tag{12}$$

The balance of dry air is computed with an equation similar to Equation (4), replacing by dry air all terms related to water. It is not presented here because its terms are null under the hypothesis that the air pressure is constant, air bubbles are considered perfectly mobile and there is no air dissolution.

Energy transfer is computed with Equation (13) and considers the energy from the various phases E_i (where i = s for the solid, i = l for the liquid and i = g for the gas phases), heat transport by advection due to liquid and mass movements, j_{Ei} (i = l for the liquid and i = g for the gas phases), heat transport by conduction given by i_c and the output or input of energy f^Q.

$$\frac{\partial}{\partial t}\left[E_s\rho_s(1 - n) + E_l\rho_l S_r n + E_g\rho_g(1 - S_r)n\right] + \nabla\cdot\left(i_c + j_{El} + j_{Eg}\right) = f^Q \tag{13}$$

The only energy flow considered is the term for heat transfer by conduction, i_c, given by Fourier's law (Equation (14)), where T is temperature and λ is thermal conductivity given by Equation (15). This conductivity considers the degree of saturation S_r of the material (Equation (2)) and is computed considering the thermal conductivities of the fully saturated and completely dried material, λ_{sat} and λ_{dry}, respectively (values in Table 3) [9].

$$i_c = -\lambda\nabla T \tag{14}$$

$$\lambda = \lambda_{sat}\sqrt{S_r} + \lambda_{dry}\sqrt{(1 - S_r)} \tag{15}$$

Finally, the numerical parameters of the model and those for the constitutive equations to which no experimental data were available were calibrated, adopting default values or following an iterative procedure [15].

4.3. Loading: Drying and Wetting

Drying and wetting were applied in the top horizontal boundary, keeping constant the exterior temperature in this boundary and in the baseline and vertical equipment walls. The temperature applied in the soil surface and in the vertical walls of the cell was equal to the average temperature of the laboratory (T^0 = 24.4 °C). Temperature changes occur due to water vapor presence diffusing through the sample (perfect gas law). These changes, affected by a constant γ_e, generate a flux of heat, given by Equation (16) [9].

$$j_{El} = \gamma_e \left(T^0 - T \right) \tag{16}$$

The drying rate depends on the relative humidity of the room, while the wetting rate is controlled by the user in the definition of the time interval to which water in a liquid phase is added. Therefore, the drying rate is controlled uniquely by the equations solved by the program, while the wetting rate can be adjusted to achieve the target suction upon drying.

Drying was simulated by applying water in the gas phase in the top horizontal boundary, creating a flow (j_g^w). The value prescribed, ${\rho_{vap}}^0 = (\rho_g \omega_g^w)^0$, was obtained from the relative humidity, RH, using Equations (11) and (12). The difference between this value and the ρ_{vap} computed with Equation (9), affected by a calibration constant β_g, generates a water flow j_g^w, given by Equation (17) [9].

$$j_g^w = \beta_g \left[\left(\rho_g \omega_g^w \right)^0 - \left(\rho_g \omega_g^w \right) \right] \tag{17}$$

It is important to highlight that a mean value of RH equal to 53% was recorded in the laboratory room during the test, but the sensor was placed around 1 m above the sample and the RH in the space close to the upper surface of the sample might be different from the recorded one. A value of RH equal to 65% was chosen in the first drying resulting from a previous sensitivity analysis performed to fit the maximum suctions measured at the tensiometers at the end of the first cycle. During the following infiltration (wetting), it seems realistic to assume a relative humidity equal to 100% in the volume of air surrounding the sample. Because the time interval between the cycles is not large enough for the RH equilibrium of all the air in the room, after the first wetting, it seems possible that the relative humidity in this environment close to the sample remains higher than the one in the room, creating a kind of a cloud. For this reason, values of RH equal to 75% have been chosen for the subsequent drying stages. This value was also found after fitting the results [15].

In the wetting phases, liquid pressure was also changed because suction decreases and becomes null if full saturation is reached (s = 0 MPa means P_l^0 = 0.1 MPa). For this reason, the flow of water in the liquid phase was also prescribed, in which the pressure difference would generate water flow given by Equation (18), with consequent water transport by conduction (Equation (5)). For P_l, a value slightly higher than that necessary to fully saturate the soil layer closer to the surface was prescribed to prevent instant evaporation [9].

$$j_l^w = (\omega_l^w)^0 \gamma_l \left(P_l^0 - P_l \right) \tag{18}$$

The values adopted for the different loads in the different surfaces are presented in Table 4. The time intervals in which each boundary condition was applied follow the experimental sequence. Constants γ_l, β_g and γ_e were defined after a sensitivity analysis made by Ponzoni [15].

Table 4. Loading conditions applied in the model.

	Soil Surface (Wetting and Drying Cycles)			Lateral Wall
	First Drying	**All Wettings**	**Further Dryings**	**All Steps**
ω_g^w (kg/kg)	0.01	0.01	0.01	0
P_g (MPa)	0.1	0.1	0.1	0
γ_g	1	1	1	0
β_g	1	1	1	0
ρ_g (kg/m^3)	1.436 (HR = 65%)	2.209 (HR = 100%)	1.661 (HR = 75%)	0
P_l (MPa)	0	0.12	0	0
γ_l	0	10	0	0
T (°C)	24.4	24.4	24.4	24.4
γ_e	4	4	4	4

With these constants, it was possible to calibrate the model, with the purpose of being able to reach the target suction at the end of each drying cycle. Other attempts to simulate wetting and drying were performed, applied in all small changes in relative humidity for drying, and a small water head for wetting. An attempt was also made to try simulating water drops from the syringe, but this would bring extra complexity and computation time without any improvement [15].

5. Results and Discussion

Figure 7 presents the comparison between experimental and numerical data concerning suction evolution along four cycles measured by both tensiometers. The arrows identify the beginning of each wetting. Overall, the model can reproduce well the average suction measured in the equipment. The steps on wetting recorded are simplified in the numerical simulation because it is almost impossible to estimate the amount of water in each water drop added to the soil using the syringe.

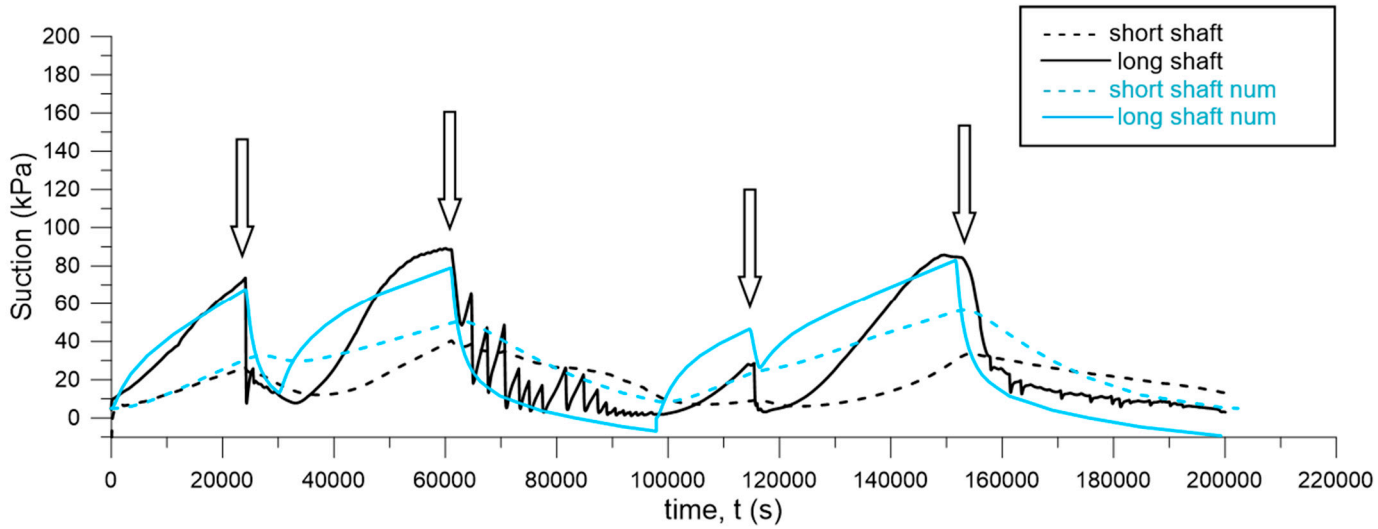

Figure 7. Comparison between numerical and experimental data measured in the two tensiometers. The arrows indicate the time steps when wetting was carried out.

As presented in Figure 7 and intended at model calibration (Tables 3 and 4), the maximum suction values measured were reproduced in almost all cycles, although the values computed for the long shaft are closer to the experimental values than those found for the short one. The shape of the drying curves for the long shaft confirms that drying occurs faster in the model than in the experiment. The shape of the curves corresponding to the small shaft is similar; however, in the model, the volume surrounding this tensiometer also appears to dry faster than in the test. The shape of the wetting curves is well reproduced,

in particular in the second wetting. There is the possibility that this can delay the response of the sensors and the interaction between their porous tips and the surrounding soil. The inclusion of the porous tips of the sensors and the characterization of this material to find the parameters will be done in the future.

The analysis of the evolution of the degree of saturation along with the test presented in Figure 8 allows for a better understanding of water balance. Wetting in the first cycle is not complete but, because the evaporation rate is low in the next, the mass of water added to the system is enough to achieve the degree of saturation at the end of the second drying. Further wettings are simulated well by the model, but the maximum values of S_r attained in the test are not reproduced. Nevertheless, the degrees of saturation after each drying computed are quite similar to the experimental values.

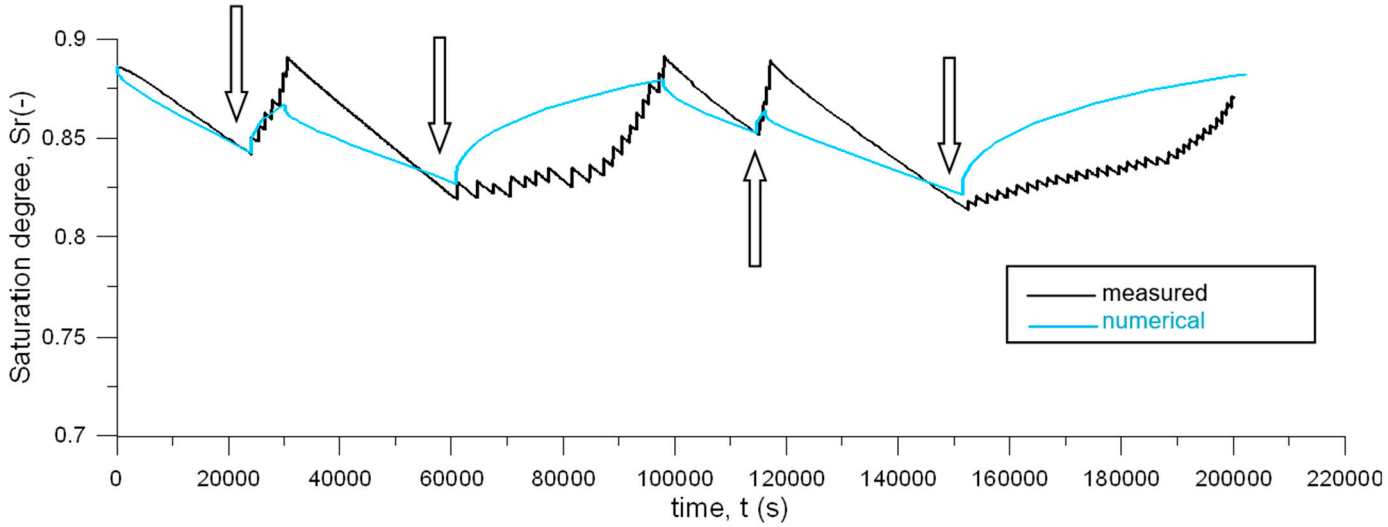

Figure 8. Comparison between numerical and experimental values for the degree of saturation in the cell. The arrows indicate the time steps when wetting was carried out.

The differences between the curves during drying may be explained by easy water transport through the unsaturated sample. When in the liquid phase (conduction), the water flow is controlled by the unsaturated permeability of the material: intrinsic permeability and parameter k_{rl} (Equation (7)). The intrinsic permeability adopted was already the smallest value measured in the tests. Higher values would lead to a significant increase in the degree of saturation upon wetting, and following drying, would not be enough to dry the sample. In addition, a sensitivity analysis of the definition of k_{rl} was unsuccessful, and therefore, the default law for this parameter was kept [15].

The relative humidity of the soil is given by parameter $\rho_{vap} = \rho_g \omega_g^w$ and was analyzed further to understand the limitations of the model to reproduce drying when dealing with vapor diffusion. The evolution of ω_g^w with the cycles is presented in Figure 9a for the two tensiometers. Vapor generation is temperature-dependent (Equations (10)–(12)), and for this reason, temperature changes must be investigated. They are presented in Figure 9b as both experimental and computed curves.

As in Figures 7 and 8, the arrows in Figure 9 identify the beginning of each wetting phase. In Figure 9a, a large increment of the amount of vapor was observed, as well as of temperature because the shape of the curves for ω_g^w and temperature is identical. Upon drying, both temperature and the amount of vapor show a sharp decrease, which explains the fast drying observed in the simulation. The shapes of the numerical curves describing suction and the amount of vapor and temperature curves are identical, confirming that vapor generation and its equilibrium control the hydraulic response of the material.

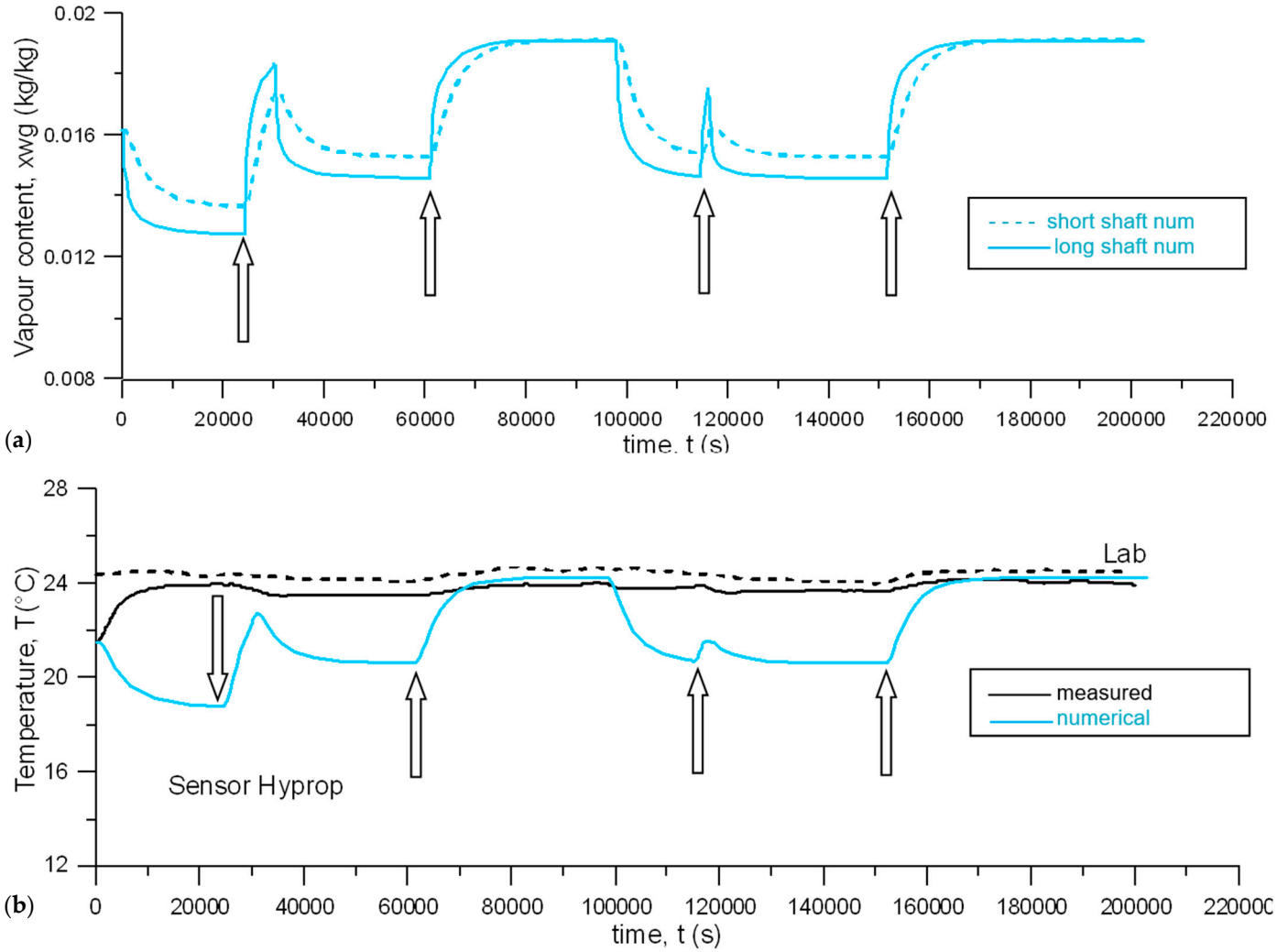

Figure 9. Analysis of vapor equilibrium considering (**a**) water vapor content computed, equal in the two tensiometers; (**b**) temperature evolution measured during the test and computed. The arrows mean wetting.

Considering Figure 9b, the comparison between the experimental and numerical curves shows important deviations. Indeed, in the test, the temperature increases in the initial drying to reach the room temperature, while it decreases in the simulation and only reaches the value measured in the room at the end of the second wetting. In addition, the amplitude of the temperature change interval is much larger in the simulation than in the room. This suggests that the value adopted for the thermal conductivity of the soil may be overestimated.

It is worth noting that there are other equations alternative to Equation (15) for the definition of thermal conductivity as a function of the degree of saturation, also considering porosity, but no improvements were obtained when using them because the soil is closer to full saturation, and therefore, all expressions lead to values closer to the saturated value λ_{sat}. For this reason, the value adopted for this constant (see Table 3) must be a relatively small value. In this case, the value adopted is near the minimum value measured in such highly porous organic materials [16,17]. This result confirms the need to perform a more adequate calibration of this variable by conceiving adequate tests.

Finally, for the suction variations and temperature intervals applied in the tests, porosity changes would be very small. Possible shrinkage would further decrease the permeability, with a small effect on the water retention curve and thermal conductivity. As discussed, this would contribute to decreasing further the water infiltration upon

wetting and increase the evaporation rate because the thermal conductivity would increase. Considering this and the fact that the porous tips were not simulated, at this stage, it can be considered that the thermohydromechanical analysis performed is sufficient for investigating this particular case.

6. Conclusions

Data recorded during the test performed using HYPROP equipment mimic the behavior observed in real dikes and provide an indication of the delayed response with depth during evaporation and infiltration. This continuous dynamic process was simulated considering a coupled thermohydraulic response. The effect of volume changes during the cycles was discarded from the analysis because the material did not show any deformation during the wetting and drying cycles. The environmental conditions were translated into numerical boundary conditions considering drying modeled only by the transport of water vapor after equilibrium with the room atmosphere, while water in the liquid phase was added upon wetting. Model calibration was performed to achieve the final suction at the end of each drying, adjusting the wetting rate.

The drying rate depends only on the relative humidity of the room and is controlled uniquely by the equations solved by the program, while the wetting rate is controlled by the user by defining the time interval to which water in the liquid phase is added. Further work must be conducted to include the porous tip of the sensors, as the thermal and hydraulic properties of this material may also contribute to the delay registered.

The simulation was able to reproduce the overall behavior observed in four complete drying–wetting cycles but the drying rate simulated was faster than the observed one. The numerical curves describing suction and the amount of vapor and temperature are identical, confirming that vapor generation and its equilibrium control the hydraulic response of the material. Vapor generation and diffusion depend on temperature; therefore, the correct characterization of the thermal properties of the material is of paramount importance when dealing with evaporation and related non-steady equilibrium problems.

Author Contributions: Conceptualization, E.P. and C.J.; Data curation, E.P. and C.J.; Formal analysis, R.C. and C.J.; Funding acquisition, C.J.; Investigation, E.P. and R.C.; Methodology, E.P., R.C. and C.J.; Resources, C.J.; Software, E.P. and R.C.; Supervision, C.J.; Validation, R.C. and C.J.; Writing—original draft, E.P. and R.C.; Writing—review and editing, R.C. and C.J. All authors have read and agreed to the published version of the manuscript.

Funding: E.P. and C.J. acknowledge the financial support on the experimental equipment of the perspective program BioGeoCivil (grant 11344) and CEAMaS (Civil Engineering Applications for Marine Sediments), supported by the European Regional Development Funding through INTERREG IV B. R.C. acknowledges financial support from the Portuguese Foundation for Science and Technology, FCT I.P., refs. SFRH/BSAB/114289/2016 and PTCDT/ECM-GEO/0728/2014.

Institutional Review Board Statement: Not applicable.

Informed Consent Statement: Not applicable.

Data Availability Statement: The raw data supporting the conclusions of this article will be made available by the authors on request.

Conflicts of Interest: The authors declare no conflicts of interest.

References

1. Hoogheemraadschap van Rijnland, H. *Flood Control in The Netherlands. A Strategy for Dike Reinforcement and Climate Adaptation*; Hoogheemraadschap van Rijnland: Leiden, The Netherlands, 2009; ISBN 978-90-72381-10-1.
2. Koelewijn, A.R.; Hoffmans, G.J.C.M.; Van, M.A. Lessons Learned from a Full-Scale Dyke Failure Test. In Proceedings of the 5th Conference of the International Conference on Case Histories in Geotechnical Engineering, New York, NY, USA, 13–17 April 2004; p. 33.
3. Tang, A.M.; Hughes, P.N.; Dijkstra, T.A.; Askarinejad, A.; Brenčič, M.; Cui, Y.J.; Diez, J.J.; Firgi, T.; Gajewska, B.; Gentile, F.; et al. Atmosphere–vegetation–soil interactions in a climate change context; impact of changing conditions on engineered transport infrastructure slopes in Europe. *Q. J. Eng. Geol. Hydrogeol.* **2018**, *51*, 156–168. [CrossRef]

4. Stirling, R.A.; Toll, D.G.; Glendinning, S.; Helm, P.R.; Yildiz, A.; Hughes, P.N.; Asquith, J.D. Weather-driven deterioration processes affecting the performance of embankment slopes. *Géotechnique* **2021**, *71*, 957–969. [CrossRef]
5. De Wolf, I.; Jommi, C. Monitoring climate induced degradation processes of soft soil dykes in the Netherlands. In Proceedings of the 7th International Conference on Geotechnical and Geophysical Site Characterization, Barcelona, Spain, 18–24 June 2024; pp. 580–586.
6. Jommi, C.; Sterpi, D.; de Gast, T.; Muraro, S.; Ponzoni, E.; van Hemert, H. Coupled Hydro-Mechanical Analysis of the Pre-failure and the Failure Behaviour of a Dyke on Soft Subsoil: Formulation and Synthesis of Results. In *Numerical Analysis of Dams*; Bolzon, G., Sterpi, D., Mazzà, G., Frigerio, A., Eds.; Springer: Cham, Switzerland, 2021; pp. 645–665.
7. Tollenaar, R.N.; van Paassen, L.A.; Jommi, C. Small-scale evaporation tests on clay: Influence of drying rate on clayey soil layer. *Can. Geotech. J.* **2018**, *55*, 437–445. [CrossRef]
8. Olivella, S.; Gens, A.; Carrera, J.; Alonso, E.E. Numerical formulation for simulator (CODE_BRIGHT) for coupled analysis in saline media. *Eng. Comput.* **1996**, *13*, 87–112. [CrossRef]
9. UPC-DLT. *CODE_BRIGHT, USER'S GUIDE*; Department of Geotechnical Engineering and Geo-Sciences, Universitat Politècnica de Catalunya: Barcelona, Spain, 2016.
10. HYPROP. HYPROP© UMS GMBH MUNICH, User Manual 2015. Available online: https://metergroup.com/products/hyprop-2/hyprop-2-support/ (accessed on 20 January 2015).
11. Decagon. *WP4 Dewpoint Potentiometer Decagon Operator's Manual*; Version 5 Decagon Devices 2007; Decagon Inc.: Pullman, WA, USA, 2007.
12. Cardoso, R.; Romero, E.; Lima, A.; Ferrari, A. A Comparative Study of Soil Suction Measurement Using Two Different High-Range Psychrometers. In *Experimental Unsaturated Soil Mechanics*; Springer: Berlin/Heidelberg, Germany, 2007; Volume 112, pp. 79–93.
13. Maček, M.; Smolar, J.; Petkovšek, A. Extension of measurement range of dew-point potentiometer and evaporation method. In Proceedings of the 18th International Conference on Soil Mechanics and Geotechnical Engineering, Paris, France, 2–6 September 2013.
14. van Genuchten, R. A closed-form equation for predicting the hydraulic conductivity of unsaturated soils. *Soil Sci. Soc. Am. J.* **1980**, *44*, 892–898. [CrossRef]
15. Ponzoni, E. Hystorical Constructions on Natural Silty Soils Accounting from the Interaction with the Atmosphere. Ph.D. Thesis, University of Brescia, Brescia, Italy, 2017.
16. Farouki. *CRREL Monograph, U.S. Army Corps of Engineers*; Cold Regions Research and Engineering Laboratory: Hanover, NH, USA, 1981.
17. Vieira, A.; Alberdi-Pagola, M.; Christoudolides, P. Characterisation of Ground Thermal and Thermo-Mechanical Behaviour for Shallow Geothermal Energy Applications. *Energies* **2017**, *10*, 2044. [CrossRef]